Live tissue intrinsic emission microscopy using multiphoton-excited native fluorescence and second harmonic generation

Warren R. Zipfel*, Rebecca M. Williams*, Richard Christie†, Alexander Yu Nikitin‡, Bradley T. Hyman†, and Watt W. Webb*§

*Department of Applied and Engineering Physics, Cornell University, Ithaca, NY 14853; †Harvard Medical School, Massachusetts General Hospital, Charlestown, MA 02129; and ‡Department of Biomedical Sciences, Cornell University, Ithaca, NY 14853

Contributed by Watt W. Webb, April 18, 2003

Multicolor nonlinear microscopy of living tissue using two- and three-photon-excited intrinsic fluorescence combined with second harmonic generation by supermolecular structures produces images with the resolution and detail of standard histology without the use of exogenous stains. Imaging of intrinsic indicators within tissue, such as nicotinamide adenine dinucleotide, retinol, indoleamines, and collagen provides crucial information for physiology and pathology. The efficient application of multiphoton microscopy to intrinsic imaging requires knowledge of the nonlinear optical properties of specific cell and tissue components. Here we compile and demonstrate applications involving a range of intrinsic molecules and molecular assemblies that enable direct visualization of tissue morphology, cell metabolism, and disease states such as Alzheimer's disease and cancer.

Multiphoton microscopy (MPM) (1, 2) is well suited for high-resolution imaging of intrinsic molecular signals in living specimens. It provides convenient excitation of the characteristic UV absorption bands of intrinsic fluorophores using IR illumination, leaving a broad uninterrupted spectral region for efficient multicolor fluorescence collection. The ability of MPM to produce images deep in optically thick preparations is crucial for intravital tissue microscopy. In addition, second harmonic generation (SHG) enables direct imaging (3) of anisotropic biological structures possessing large hyperpolarizabilities, such as collagen (4, 5). These imaging modalities are easy to implement simultaneously and differ only in optical filter selection and detector placement.

To date, most biological MPM has depended on labeling with conventional fluorophores or fluorescent proteins such as the GFPs; however, a few studies have used two-photon excitation (2PE) of intrinsic molecules such as NAD(P)H (6–8) and flavins (9), three-photon excitation (3PE) of serotonin (10–12), and SHG of collagen, skeletal muscle, and microtubules (2, 13). The combination of intrinsic and extrinsic signals is particularly powerful. For example, the process of tumor cell migration along collagen fibers can be observed by using GFP-labeled tumor cells and intrinsic collagen SHG (14). 2PE fluorescence spectra currently exist for NAD(P)H and some flavins (9, 15), and 3PE spectra exist for serotonin, tryptophan, and dopamine (10). Here we report the SHG efficiency spectrum for various collagens and 2PE cross sections of a "basis set" of tissue 2PE fluorophores. We demonstrate μm-resolution multiphoton imaging of normal tissue structure and of disease states such as Alzheimer's disease (AD) and cancer. Intrinsic emission MPM in living specimens yields detail that may ultimately prove useful to clinical diagnostics as well as to basic biological research.

Materials and Methods

Instrumentation and the associated methodologies used in these investigations are described in detail in *Supporting Materials and Methods*, which is published as supporting information on the PNAS web site, www.pnas.org. The multiphoton microscopes consisted of modified Bio-Rad laser scanning instruments with laboratory-built detection systems and fsec Spectra-Physics titanium sapphire lasers as the excitation sources. *In vivo* emission spectra of multiphoton-excited fluorescence or SHG of intrinsic components were generated by scanning small regions of the specimen and focusing the emission into a Spex model 270M spectrometer (Jobin Yvon, Edison, NJ) with a cooled charge-coupled device detector. Spectra were corrected for the grating and detector efficiency. 2PE cross sections were measured by comparison to 10 μM fluorescein as a reference compound. Rodent tissues were excised and incubated for no longer than 1 h in glucose-containing buffered saline solution before imaging. The human skin explants (Fig. 3 *b* and *c*) were fast-frozen plugs. Brain specimens (Fig. 4 *a–d*) were fresh blocks of tissue from autopsy incubated in cold buffered saline solution for no longer than 12 h. For confirmatory immunohistochemistry, neurofibrillary tangle (NFT) location was marked by ablating small spots in the tissue. The block was then fixed and sectioned, and immunohistochemistry was performed by using paired helical filament (PHF)-τ primary (graciously provided by Peter Davies, Albert Einstein College of Medicine, New York) and FITC secondary antibodies. NFTs were then relocated using the ablation marks and imaged by confocal microscopy. Specimens for histological comparisons were prepared by using standard methods and tumor diagnoses were carried out by one of us (A.Y.N.) according to the Annapolis classification (16). Unless otherwise stated, multicolor images were acquired at 750 nm ($\approx$100-fs pulsewidth) and displayed with fluorescence in grayscale and SHG in green pseudocolor.

Results and Discussion

Intrinsic Fluorophores. Because molecular emission spectra are generally independent of the photon order of excitation, the interpretation of multiphoton tissue images initially relies on the large body of one-photon excitation (1PE) spectroscopy and imaging experiments (17). Tissue fluorophores are primarily derived from the aromatic amino acids such as Trp, Tyr, and Phe (UV emission) and from vitamin derivatives which emit at longer wavelengths (400–600 nm). Examples of the latter include retinol, riboflavin, the nicotinamide ring of NAD(P)H derived from niacin, or the pyridolamine crosslinks found in elastin and some collagens (18), which are based on pyridoxine (vitamin B6).

Fig. 1*a* shows 2PE action cross sections of several fluorescent vitamin derivatives. Because these values are orders of magnitude lower than typical extrinsically added fluorophores (15), intrinsic fluorescence imaging generally requires higher illumi-

Abbreviations: NADH, nicotinamide adenine dinucleotide; MPM, multiphoton microscopy; 2PE, two-photon excitation, 3PE, three-photon excitation; SHG, second harmonic generation; NFT, neurofibrillary tangle; AD, Alzheimer's disease.

§To whom correspondence should be addressed at: Cornell University, 212 Clark Hall, Ithaca, NY 14853. E-mail: www2@cornell.edu.

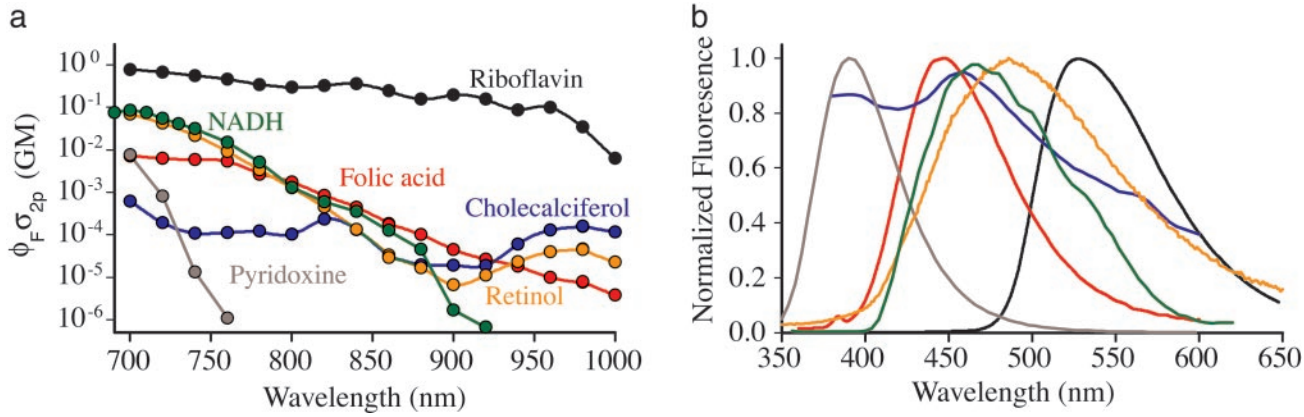

Fig. 1. Two-photon action cross sections and emission spectra from a basis set of biological molecules. (*a*) Action cross sections (absorption cross section multiplied by the fluorescence quantum yield) of six molecules that contribute much of the intracellular 2PE intrinsic fluorescence. Units: 1 GM (Göppert-Mayer) equals 10^{-50}·cm^4 s. All compounds were measured in buffered (pH 7.2) saline solution, except retinol and cholecalciferol (vit D), which were measured in EtOH. Riboflavin, cholecalciferol, and NADH were measured at 100 μM; retinol, folic acid, phylloquinone, pyridoxine, and nicotinamide were measured at 500 μM. (*b*) Emission spectra of the compounds shown in *a* (measured in the same solvents).

nation intensities than would be required for MPM with conventional probes. However, protein binding or association with membranes or lipid droplets may enhance the *in vivo* fluorescence quantum yield. In addition, many autofluorophores are found at extremely high concentrations; for example, indoleamine concentrations within secretory granules are ≈50 mM (10, 11). Within the Ti:Sapphire (Ti:S) laser tuning range, the 2PE cross sections are maximal between 700 and 750 nm, and therefore intrinsic imaging is usually carried out in this range. This wavelength dependence explains why multiphoton imaging at <800 nm has been reported to be more damaging (19), with or without any added fluorophores. Excitation of intrinsic species often cannot be avoided and maximized collection efficiency is crucial for maintaining the minimal excitation dose to minimize photodamage. For functional imaging, doses at 20 mW/μm^2 (a few mW at high NA) with a beam dwell time of ≈1 μsec are generally safe (8, 11).

Fig. 1*b* shows the emission spectra of the molecules whose action cross sections were reported in Fig. 1*a*. These spectra demonstrate that discrimination between sources of intrinsic fluorescence is often difficult and cannot be based on emission wavelength alone. Much of the intrinsic fluorescence observable with MPM is in the 440- to 500-nm range, and verification of the source of a particular emission often requires additional information, such as knowledge of the tissue's biochemical composition, additional immunohistochemistry, colocalization with organelle stains, or fluorescence decay time measurements.

Cellular Sources of Intrinsic Emissions. The primary intracellular sources of fluorescence are NAD(P)H, flavins, retinol, and tryptophan and its indoleamine derivatives. Indoleamines, such as serotonin (5-HT) and melatonin, have 1PE absorption maxima at wavelengths <300 nm with emission at 340 nm, requiring 3PE between 700 and 800 nm (10). Serotonin-containing granules in cultured mucosal mast cells can be directly imaged to follow both 5-HT uptake and stimulated exocytosis (11). Indoleamine pools can be imaged *in vivo* as well. For example, indoleamine-containing granules in a mouse pineal gland are identified by imaging the UV emission (Fig. 2*a Right*). The proximal choroid plexus (Fig. 2*a Left*) shows a uniform intracellular Trp pattern suggestive of the general protein distribution (10, 11). In addition to serotonin, other indoleamines including melatonin and the 5-HT oxidation products 5-hydroxyindole acetic acid (5-HIAA) and 5-hydroxytryptophol (5-HTOL), are found in high concentrations in various living tissues (20) and, if present, would be observable *in vivo* within the same wavelength range (see Table 1). Although the subcellular localization of melatonin (and 5-HT) in pinealocytes is still unresolved; the direct imaging approach demonstrated here (Fig. 2*a Inset*) corroborates immunohistochemical and cell fractionation studies that indicate that indoleamines are located in the nucleus in pinealocytes (21).

In pinealocytes, blue fluorescence (≈400–490 nm) arises in separate punctate regions (Fig. 2*b Right*). A major source of intracellular blue emission is NAD(P)H/NAD(P)+, which is fluorescent only when reduced. Nicotinamide adenine dinucleotide (NADH) fluorescence has long been used as an indicator of cellular metabolic state (22, 23). In neurons (data not shown) and pancreatic beta cells (7), the punctate blue fluorescence originates primarily from mitochondrial NAD(P)H. Flavins fluoresce yellow in their oxidative states, and, in some tissues, FAD and NAD(P)H together can provide ratiometric mapping of cellular redox state (9, 23, 24). In epithelial cells of the choroid plexus (Fig. 2*b Left*), the uniform blue fluorescence is due, at least in part, to the high concentrations of protein-bound retinol (25), rather than solely of NAD(P)H. By using antibodies against retinol-binding protein (RBP), we have found that the same general regions that exhibit blue fluorescence *in vivo* also stain positive for RBP (data not shown).

Distinct UV and blue emission patterns of microvilli in the small intestine of mouse are shown in Fig. 2 *c* and *d*. The UV fluorescence (Fig. 2*c*) again shows a uniform Trp background with a few bright punctate spots, possibly indicating indoleamine storage, whereas the blue fluorescence (Fig. 2*d*) clearly delineates the structure of the epithelial cells (*Inset*). In ovarian epithelial cells (Fig. 2*e*) and in the granulosa cells (arrowhead) and oocytes (O) of the developing follicle, blue fluorescence, presumably because of NAD(P)H, again delineates the cellular regions. Thecal cells (T) surrounding follicles show punctate regions of green-yellow fluorescence of an unknown origin, whereas the corpus luteum (CL) emits bright blue fluorescence compared with other stromal cells. Although studies have shown that luteal cells can contain high levels of NAD(P)H (26), the fluorescence also occurs because of the high concentration of retinol found in this tissue (27). Our signal level is consistent with published retinol concentrations (27) and its 2PE action cross section (Fig. 1*a*). Furthermore, the luteal intrinsic fluorescence remains even after fixation, which generally destroys NAD(P)H fluorescence. Fig. 2 *e* and *f* demonstrate the similarity of MPM

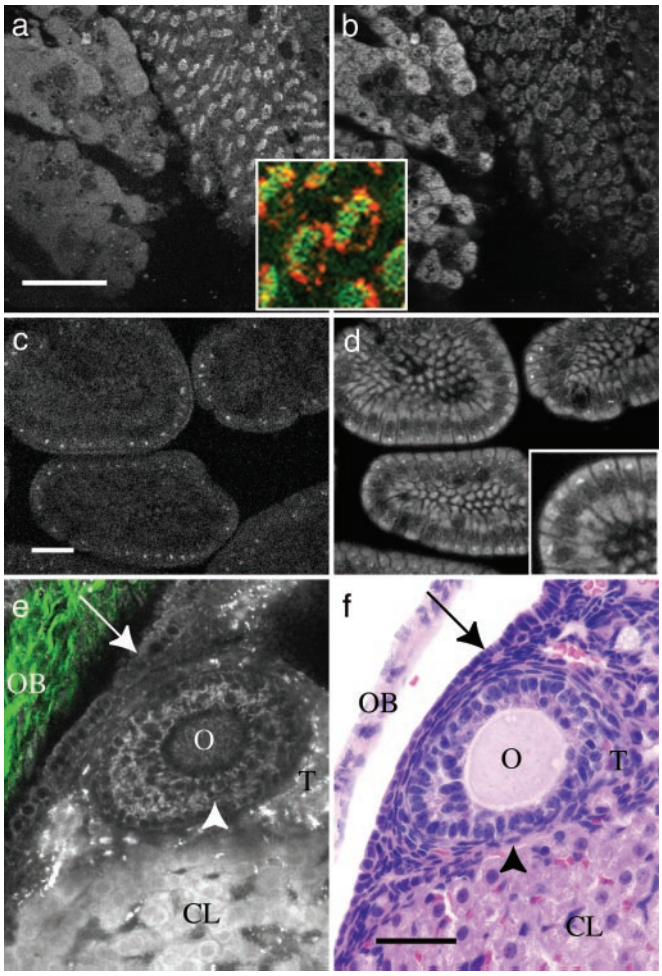

Fig. 2. Intrinsic intracellular fluorescence sources. (*a*) 3PE emissions (<400 nm) show intracellular Trp in the choroid plexus (*Left*) and indoleamines in the pineal gland (*Right*) of a mouse. (*b*) 2PE-generated blue emissions (400–500 nm, presumably NADH). (*Inset*) A higher zoom image of the pinealocytes in *a* and *b* with the UV emission (green pseudocolor) and blue emission (red pseudocolor) merged to show they do not colocalize. (*c*) In the microvilli of the small intestine, uniform 3PE UV emission indicates the general protein distribution with punctate regions, suggesting indoleamine storage. (*d*) The blue emission is sufficient for discrimination between epithelial and goblet cells in the intestinal villi. MPM image (fluorescence in grayscale, SHG in green; *e*) and hematoxylin/eosin-stained histological images of a mouse ovary (*f*). The ovarian epithelium (arrow), oocyte (O), granulosa cells (arrowhead), thecal cells (T), the corpus luteum (CL), and ovarian bursa (OB) are all clearly resolvable and resemble the histological image in *f*. (Scale bars, 50 μm.)

images of an intact ovary to standard histological images of the same tissue after fixation, sectioning, and conventional staining.

Extracellular Sources of Intrinsic Emissions. Elastin and collagen, visualized by 2PE and SHG respectively, are the two primary extracellular sources of nonlinear emissions, and are both, for example, clearly evident in optical sections of an intact arteriole (Fig. 3*a*). The characteristic elastin ring lies directly under the endothelial cell lining, whereas collagen I and III fibrils are dispersed among the smooth muscle cells and form a dense mesh surrounding the vessel (green in Fig. 3*a*). Sixty percent of the amino acids in elastin are nonpolar (28), with lysine-residue-linked pyridinoline groups forming covalent cross links between the chains, producing a globular conformation. Pyridinoline groups exhibit an ≈400-nm emission maximum (29) when excited in the UV and may be responsible for this 2PE elastin

Table 1. Multiphoton excitation (MPE) characteristics of intrinsic emitters in the 700- to 1,000-nm range

Molecule	Process	λ_{ex} 50% max, nm*	Cross section	MPE, refs.†
Tyrosine	3PE	<700	1×10^{-84}	10
Tryptophan	3PE	700–740	1×10^{-84}	10
Serotonin	3PE	700–720	4×10^{-84}	10
Melatonin	3PE	700–720	7×10^{-84}	
5-HIAA	3PE	700–720	2×10^{-84}	
5-HTOL	3PE	700–720	5×10^{-84}	
Retinol	2PE	700–830	7×10^{-52}	
Flavins	2PE	700–730	$1–8 \times 10^{-51}$	9, 13
NADH	2PE	690–730	9×10^{-52}	6–9, 13
Pyridoxine	2PE	690–710	8×10^{-53}	
Folic acid	2PE	700–770	7×10^{-53}	
Cholecalciferol	2PE	<700	6×10^{-54}	
Elastin	2PE	700–740	—	
NFTs	2PE	700–780	—	
Lipofuscin	2PE	700–850	High‡	
Collagen	SHG	700–740	—	41
Microtubules	SHG	—	—	13
Skel. muscle	SHG	—	—	13

2PE-action cross sections given for 700-nm excitation, units are cm^4 s; 3PE cross sections measured at 720 nm, units are $cm^6 \cdot s^2$. (For comparison to Fig. 1: $10^{-50} \cdot cm^4$ s = 1 GM for 2PE cross sections. There is no unit equivalent to the GM for 3PE cross sections.)

*The Ti:S wavelength range where the cross section is >50% of the peak value.

†Listed values include results from previously published work. We note, however, that our collagen SHG efficiency spectrum differs significantly from ref. 41.

‡Varies according to type.

fluorescence (18). *In vivo* spectra (Fig. 3*d*) obtained from 2PE of elastin fibers in human skin (Fig. 3*b*) exhibit a small peak at ≈400 nm, but the emission maximum of 480 nm resembles that from elastin powder and may correspond to pyridinoline aggregates (17).

Fig. 3*c* shows the collagen SHG signal collected from the same skin sample excited at 800 nm, away from the elastin excitation peak. Collagen SHG is strongest when the illumination polarization is parallel to the fibrils (5, 30), resulting in SHG with the same polarization. With MPM imaging in tissue, collagen SHG acts as a "tissue map," clearly defining boundaries between different tissues and cells within the extracellular matrix. Through comparison to histological and biochemical literature to identify specific collagen types present in different tissues, we have found that SHG is produced by a wide variety of collagens. We have imaged the primary fibrillar collagens as follows: collagen I (tendon in Fig. 3*e*, bone in Fig. 3*k*), collagen II (articular cartilage in Fig. 3*f*), and mixtures of collagens I and III (blood vessels in Fig. 3*a*, dermis in Fig. 3*c*, and tendon sheathing in Fig. 3*e*). We have been unable to image nonfibrillar collagens such as collagen IV by SHG. We have also not observed SHG from elastin fibers or other extracellular matrix components such as fibronectin or laminin.

SHG is a nonlinear coherent scattering process that conserves energy, and therefore the SHG wavelength (λ_{SHG}) is always half the illumination wavelength (λ_I). The SHG spectra (Fig. 3*g*) from rat tendon illuminated at several different wavelengths (Fig. 3*h*) exhibit this $\lambda_I/2$ dependence and a spectral width that scales as $1/\sqrt{2}$ of the illumination spectral width (as expected from sum-frequency generation across the fundamental's spectrum). In rat tail tendon we see essentially no 2PE fluorescence (arrow in Fig. 3*g*) relative to the SHG intensity, although induced fluorescence can arise with too much illumination. This observation (SHG intensity ≫ 2PE fluorescence) holds for all types

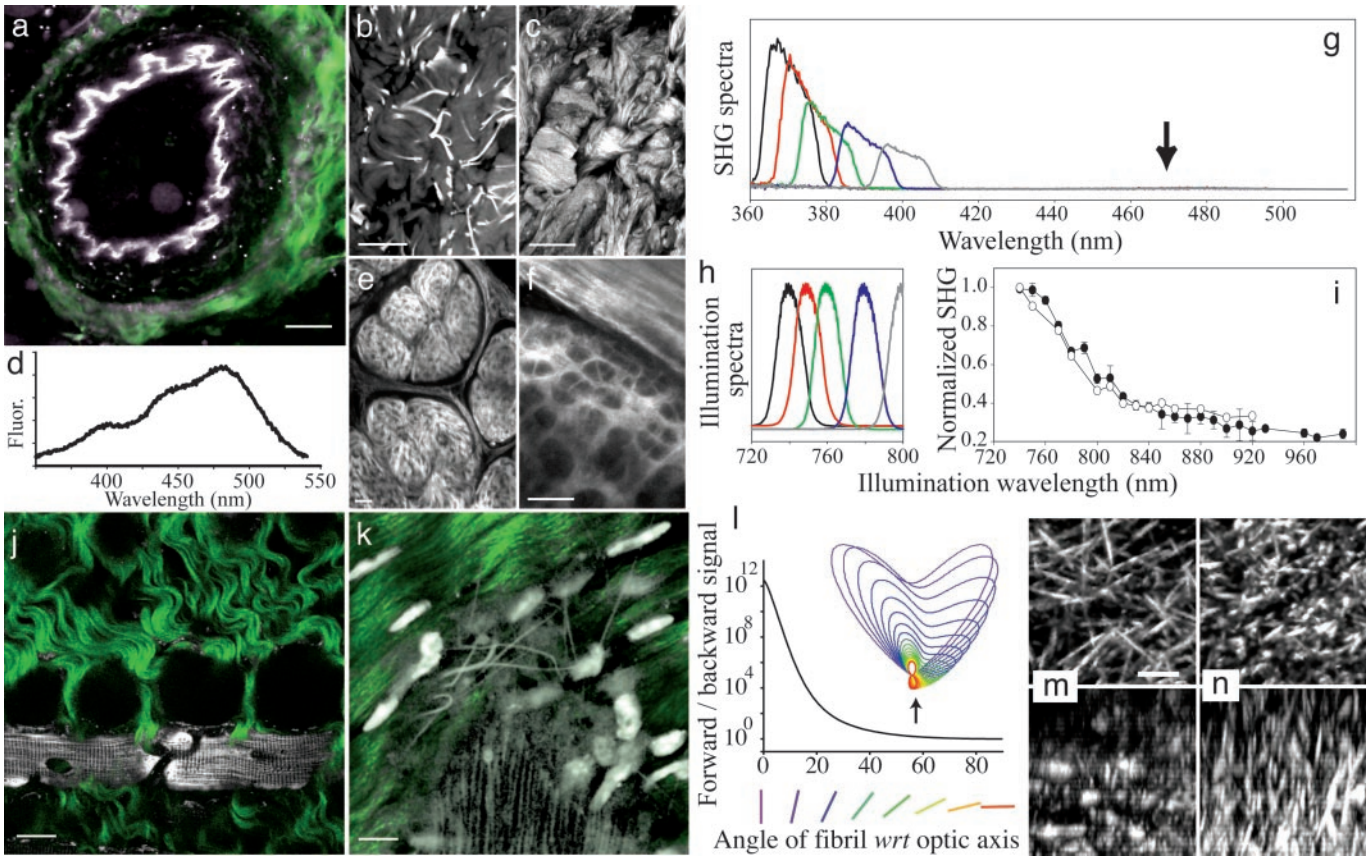

Fig. 3. Extracellular emission sources. (*a*) Mouse arteriole with a fluorescent elastin lining (grayscale) and surrounded by collagen (SHG in green pseudocolor; scale bar, 20 μm). Elastin fibers from a human skin explant (740 nm; *b*) and SHG image (*c*) showing only collagen structure taken at 800 nm to avoid the elastin absorption. (*d*) *In vivo* spectrum collected from *b*. (*e*) SHG image of rat tail tendon. (*f*) SHG image of the articular cartilage-meniscus junction in mouse. *In vivo* SHG emission spectra from rat tail tendon (*g*) with different (color-coded) excitation wavelengths (*h*). 2PE fluorescence was not evident (arrow). (*i*) Relative SHG cross section for rat tendon (○) and a pure collagen I gel (●). (*j*) Collagen scaffolding (SHG, green) surrounding a cardiac myocyte (NAD(P)H, grayscale) in a mouse heart (740-nm excitation). (*k*) Collagenous periosteum (green) and calcein-loaded osteoblast precursors (grayscale) in a mouse femur imaged at 920 nm (SHG at 460 nm, 520-nm calcein emission). (*l*) F/B SHG as a function of fibril angle to the optical axis. (*Inset*) The expected SHG intensity profiles from variously oriented rods. (*m*) Backward-directed SHG image of an ≈10-μm-thick collagen gel (*Upper*, lateral projection; *Lower*, axial projection; scale bar, 5 μm). (*n*) Forward-directed SHG from the same collagen gel.

of collagen-containing tissues examined. The wavelength dependence of SHG from rat tendon and a purified collagen I and III gel (Fig. 3*i*) are identical, increasing toward the 700- to 800-nm region, presumably because of two photon absorption resonance effects (expected max ≈560 nm). The measured SHG spectra (Fig. 3*g*) also reflect the wavelength dependence of the process (Fig. 3*i*). At wavelengths <800 nm, the "bluer" regions of the illuminating spectrum give significantly more SHG than the "redder" regions. Although collagen SHG efficiency is higher in the 700- to 800-nm region, in practice we can image significantly deeper in the 900-nm region, presumably due to less scattering of the 450-nm SHG than light <400 nm.

The ability to shift λ_{SHG} by tuning λ_I has practical implications for tissue imaging because SHG can always be distinctly separated from other emissions. For example, in Fig. 3*j* the banding pattern produced by mitochondrial NADH in a cardiac myocyte (grayscale) in freshly excised heart tissue is clearly distinguishable from its collagen scaffolding (green). In the periosteum from a young mouse femur (Fig. 3*k*), osteoblast precursors loaded with calcein can be visualized within the collagenous matrix.

Emitted SHG is generally anisotropic because of phase matching constraints of coherent scattering. If the size of the scattering structure along the optical axis is $\gg\lambda_I$, the SHG is primarily forward directed; whereas if it is much less, forward (F) and backward (B) SHG are equal. This rule holds true for single-photon scattering (Mie vs. Rayleigh; ref. 31) as well as SHG (3, 32) and other nonlinear scattering processes (33). Thus, F/B decreases by orders of magnitude as fibrils become less aligned with respect to the optical axis. Fig. 3*l* shows theoretical SHG intensity profiles from a focused beam impinging on thin rods of parallel-induced dipoles (calculated by following ref. 34); the plot shows integrated F/B as a function of rod orientation. Experimental verification is shown in images of simultaneously collected backward- and forward-directed SHG from an optically thin collagen gel (fibril length ≈10 μm), demonstrating that vertically oriented fibrils scatter mostly forward (Fig. 3*m*), whereas laterally oriented fibrils scatter bidirectionally (Fig. 3*n*). With a focused beam and scatterer size of $\approx\lambda_I$ or greater, the forward-directed emission profile is further influenced by the Gouy phase anomaly and the orientation and distribution of scatterers (32, 34). The existence of backward scattering in tissue is fortuitous for *in vivo* tissue imaging because collecting forward propagating signal is impractical in many cases.

Intrinsic Signals from Diseased Tissue. Changes in the intensity of intrinsic fluorescence, induction of new emissions by cross-linking of proteins or of proteins and lipids, and morphologic changes in collagen structure imaged by SHG, can all be intrinsic indicators of disease states. Examples of disease-induced intrin-

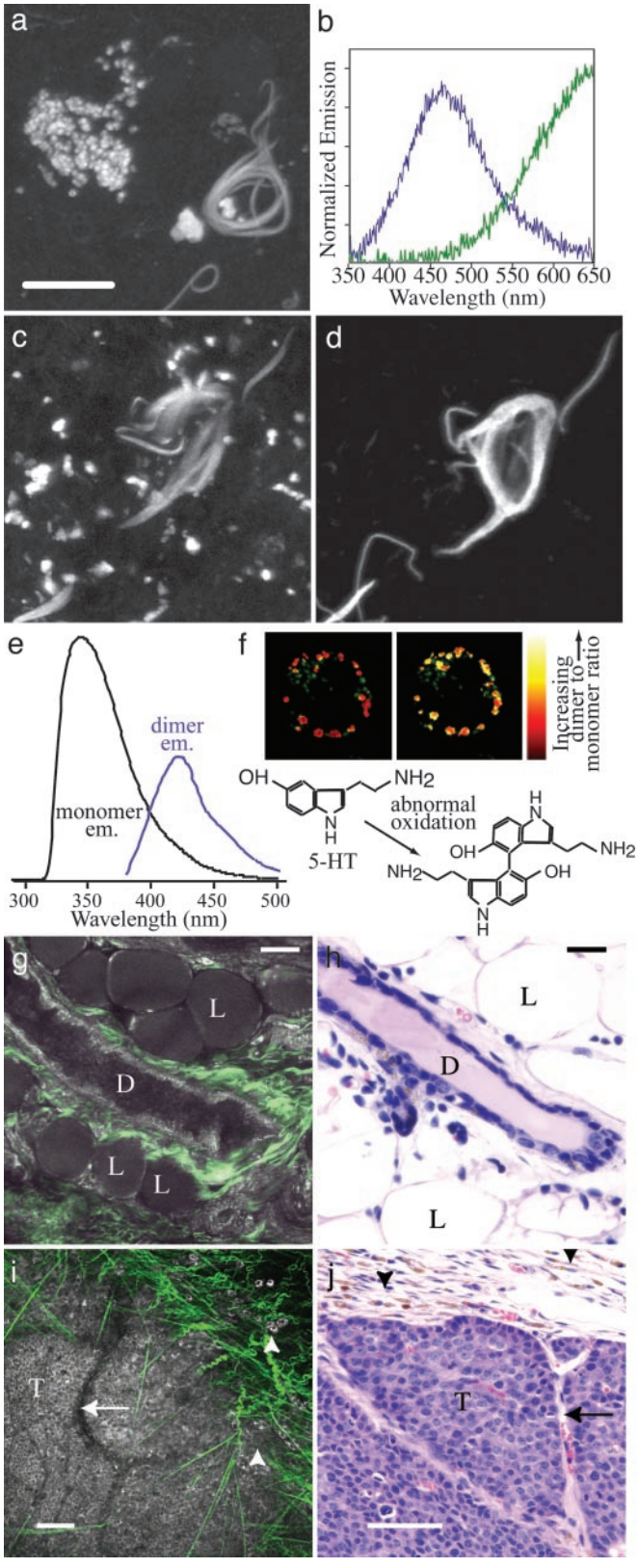

Fig. 4. Examples of intrinsic fluorescence associated with disease-driven aggregation and oxidative stress. (*a*) NFTs of AD in unfixed tissue exhibit blue fluorescence (740-nm excitation, blue spectrum in *b*; scale bar, 10 μm). Granular structure is lipofuscin (green spectrum in *b*). A single autofluorescent NFT (*c*) and the same tangle stained with FITC/PHF-τ antibodies (*d*). (*e*) Serotonin is readily oxidized, forming blue and green mulitmers. (*f*) Serotonin-loaded granules in RBL-2H3 cells before and after a 5-min exposure to 1 μM hydrogen peroxide. (*g* and *h*) Intrinsic emission (750-nm excitation; *g*) and histological images of a normal mammary gland (*h*). The duct (D), composed of epithelial cells, exhibits punctate intracellular fluorescence (grayscale) and is surrounded by collagen scaffolding (green) and lipid-containing adipocytes (L). Intrinsic fluorescence (*i*) and histological (*j*) imaging of mammary carcinoma in a 230-day-old *TgN(MMTVneu)202Mul* mouse. Shown are monomorphous polygonal tumor cells (T) with few vessels (arrow) and virtually no collagen. Note loose collagenous stroma (green) at the tumor edge; cells between collagen fibers are hemosiderin-laden macrophages (arrowheads). *h* and *j* were prepared with hematoxylin-eosin staining. (Scale bars, 40 μm.)

sic signals are shown in Fig. 4, where the use of 2PE, 3PE, and SHG is essential.

AD. We investigated the possibility that the fibrillar structures associated with AD, β-amyloid, and the τ-filaments in NFTs might exhibit autoflourescent signatures under 2PE. In particular, dityrosine and tyrosine oxidation products have been implicated in AD pathophysiology (35). To test for these types of disease signatures, we examined tissue from cortical and hippocampal regions taken at autopsy from AD patients. Control blocks were stained for β-amyloid plaque and NFTs with thioflavin-S, whereas blocks from paired adjacent regions were imaged without staining. Although unstained plaques did not exhibit any detectable autofluorescence, NFTs displayed a surprising intrinsic fluorescence under 2PE at 700–800 nm (Fig. 4*a*) in all five AD cases examined. The spectrum of an individual NFT shows an emission peak at 460 nm (Fig. 4*b*), which is redder than would be expected from ditryosine alone (400-nm emission) and occurs possibly because of higher-order polymerized tyrosine products (36). Lipofuscin granules are also brightly fluorescent but have an emission spectrum easily distinguishable from NFT emission (Fig. 4*b*). The specimens were then fixed and stained with PHF-τ antibodies, a standard method for identifying NFTs. The same autofluorescent structures found in the fresh tissue (Fig. 4*c*) were relocated in the fixed tissue, imaged by confocal microscopy, and found to correspond to PHF-τ immunoreactive structures (Fig. 4*d*).

Polymerized Indoleamines. By using MPM it is also possible to detect aberrant indoleamines. Normally, excess 5-HT is enzymatically converted to compounds such as 5-HIAA, one of several stable oxidized forms of indoleamine. Under conditions of oxidative stress, polymerized products of indoleamine oxidation can form and have been implicated in the etiology of neurodegenerative diseases such as AD, several psychotic diseases, and the neurodegenerative effects of amphetamines (37). The primary aberrant oxidation products of 5-HT, such as tryptamine diones, undergo rapid dimerization resulting in fluorescent compounds colocalized with the monoamine pool. The resulting dimers have absorption bands in the 350-nm range and emission at $\approx$420 nm (Fig. 4*e*). By using simultaneous 3PE of 5-HT (UV emission) and 2PE of dimers (blue emission) it is possible to image changes in the oxidative state of granule-residing indoleamines. As an example, Fig. 4*f* shows a change in the ratio of blue to UV emission in 5-HT granules in mucosal mast cells induced by peroxide-induced oxidative stress.

Cancer. MPM is already an important tool for cancer research (14, 38), and intrinsic emission MPM has promise as a clinical diagnostic technique. Intrinsic fluorescence can often be used to distinguish dysplastic and neoplastic tissue from normal tissue (17), with the most useful differences between normal and cancerous tissue found by using UV excitation of NADH and collagen. An alternative is to use MPM in the 740- to 780-nm range, where NAD(P)H fluorescence (460 nm) and collagen SHG (370–390 nm) are easily observable. We tested the poten-

tial of this approach on a model of mammary carcinogenesis in Tg*N(MMTVneu)202Mul* transgenic mice (39). The normal mammary gland (Fig. 4 *g* and *h*) and mammary tumor (Fig. 4 *i* and *j*) were imaged either directly with MPM (Fig. 4 *g* and *i*) or after routine histological processing (Fig. 4 *h* and *j*). Ducts and fibrous and adipose tissue were recognizable by both methods in the normal mammary gland. The mammary carcinoma was characterized by solid sheets of epithelial cells with few vessels, very little intratumoral stroma, and intensive peripheral infiltration with hemosiderophages. MPM demonstrated the absence of significant accumulation of collagen within the tumor, a feature not evident in the conventionally prepared specimen. MPM allows for imaging at resolutions equal to those of standard histopathology, but also provides additional complementary information about neoplastic processes. These observations provide rationale for using MPM in animal models, as well as for further developing its diagnostic potential.

Conclusions

Intrinsic emission MPM enables three-dimensional, sub-μm resolved imaging of unstained living tissue. Although excitable at >700 nm, most intrinsic fluorophores maximally absorb <700 nm (Fig. 1) and exhibit broad blue fluorescence. SHG in tissue arises primarily from collagen (5) and to a lesser degree from microtubules and skeletal muscle (13). Table 1 summarizes the MPE characteristics of cell and tissue components accessible in the 700- to 1000-nm wavelength region. These nonlinear intrinsic emissions can produce highly detailed images providing information on general tissue morphology, redox state [by means of NAD(P)H, flavins, or degree of indoleamine oxidation] and subresolution determination of collagen fibril orientation and width (through SHG directionality).

The proliferation of multiphoton microscopes in research settings ensures continued investigation and application of intrinsic tissue imaging in biological research, particularly in studies of model systems of disease. MPM should also prove useful as an effective alternative to standard histopathological preparations for rapid examination of fresh biopsies. Finally, the recent discovery that it is possible to propagate fsec pulses efficiently through microstructured optical fibers (40), suggests that multiphoton endoscopy may eventually be used to produce detailed intrinsic fluorescence spectra and images of tissues at the cellular level from deep within living animals or even human patients.

We thank K. Kasischke, H. Vishwasrao, D. Dombeck, C. Farnum, and A. Flesken-Nikitin for expertise and discussion. W.R.Z., R.M.W., and W.W.W. were supported by National Institutes of Health–National Institute for Biomedical Imaging and Bioengineering Grants 9-P41-EB0011976-16 and NCI R33-645644; A.Y.N. was supported by National Institutes of Health Grants CA96823-01, DOD BC991016, and PC010342; and B.T.H. and R.C. were supported by National Institutes of Health Grant AG08487.

1. Denk, W., Strickler, J. H. & Webb, W. W. (1990) *Science* **248,** 73–76.
2. Williams, R. M., Zipfel, W. R. & Webb, W. W. (2001) *Curr. Opin. Chem. Biol.* **5,** 603–608.
3. Freund, I. & Deutsch, M. (1986) *Opt. Lett.* **11,** 94–96.
4. Fine, S. & Hansen, W. P. (1971) *Appl. Opt.* **10,** 2350–2553.
5. Freund, I., Deutsch, M. & Sprecher, A. (1986) *Biophys. J.* **50,** 693–712.
6. Piston, D. W., Kirby, M. S., Cheng, H. P., Lederer, W. J. & Webb, W. W. (1994) *Appl. Opt.* **33,** 662–669.
7. Patterson, G. H., Knobel, S. M., Arkhammar, P., Thastrup, O. & Piston, D. W. (2000) *Proc. Natl. Acad. Sci. USA* **97,** 5203–5207.
8. Bennett, B. D., Jetton, T. L., Ying, G., Magnuson, M. A. & Piston, D. W. (1996) *J. Biol. Chem.* **271,** 3647–3651.
9. Huang, S. H., Heikal, A. A. & Webb, W. W. (2002) *Biophys. J.* **82,** 2811–2825.
10. Maiti, S., Shear, J. B., Williams, R. M., Zipfel, W. R. & Webb, W. W. (1997) *Science* **275,** 530–532.
11. Williams, R. M., Shear, J. B., Zipfel, W. R., Maiti, S. & Webb, W. W. (1999) *Biophys. J.* **76,** 1835–1846.
12. Williams, R. M. & Webb, W. W. (2000) *J. Cell Sci.* **113,** 3839–3850.
13. Campagnola, P. J., Mohler, W. & Millard, A. E. (2002) *Biophys. J.* **82,** 493–508.
14. Wang, W. G., Wyckoff, J. B., Frohlich, V. C., Oleynikov, Y., Huttelmaier, S., Zavadil, J., Cermak, L., Bottinger, E. P., Singer, R. H., White, J. G., *et al.* (2002) *Cancer Res.* **62,** 6278–6288.
15. Xu, C., Zipfel, W., Shear, J. B., Williams, R. M. & Webb, W. W. (1996) *Proc. Natl. Acad. Sci. USA* **93,** 10763–10768.
16. Cardiff, R. D., Anver, M. R., Gusterson, B. A., Hennighausen, L., Jensen, R. A., Merino, M. J., Rehm, S., Russo, J., Tavassoli, F. A., Wakefield, L. M., *et al.* (2000) *Oncogene* **19,** 968–988.
17. Richards-Kortum, R. & Sevick-Muraca, E. (1996) *Annu. Rev. Phys. Chem.* **47,** 555–606.
18. Deyl, Z., Macek, K., Adam, M. & Vancikova, O. (1980) *Biochim. Biophys. Acta* **625,** 248–254.
19. Konig, K., Liang, H., Berns, M. W. & Tromberg, B. J. (1996) *Opt. Lett.* **21,** 1090–1092.
20. Sirotkin, A. V. & Schaeffer, H. J. (1997) *J. Endocrinol.* **154,** 1–5.
21. Menendez-Pelaez, A. & Reiter, R. J. (1993) *J. Pineal Res.* **15,** 59–69.
22. Chance, B., Cohen, P., Jobsis, F. & Schoener, B. (1962) *Science* **137,** 499–507.
23. Mironov, S. L. & Richter, D. W. (2001) *J. Physiol.* **533,** 227–236.
24. Combs, C. A. & Balaban, R. S. (2001) *Biophys. J.* **80,** 2018–2028.
25. Macdonald, P. N., Bok, D. & Ong, D. E. (1990) *Proc. Natl. Acad. Sci. USA* **87,** 4265–4269.
26. Szabadkai, G., Pitter, J. G. & Spat, A. (2001) *Pflügers Arch.* **441,** 678–685.
27. Stacewicz-Sapuncakis, M., Chang Wang, H. H. & Gawienowski, A. M. (1975) *Biochim. Biophys. Acta* **380,** 264–269.
28. Cleary, E. G. & Gibson, M. A. (1996) in *Extracellular Matrix*, ed. Comper, W. D. (Harwood, London), Vol. 2, pp. 95–140.
29. Bridges, J. W., Davies, D. S. & Williams, R. T. (1966) *Biochem. J.* **98,** 451–468.
30. Stoller, P., Reiser, K. M., Celliers, P. M. & Rubenchik, A. M. (2002) *Biophys. J.* **82,** 3330–3342.
31. Born, M. & Wolf, E. (1980) *Principles of Optics* (Pergamon, Oxford).
32. Mertz, J. & Moreaux, L. (2001) *Opt. Commun.* **196,** 325–330.
33. Volkmer, A., Ji-Xin, C. & Xie, X. S. (2001) *Phys. Rev. Lett.* **87,** 023901-1–023901-4.
34. Moreaux, L., Sandre, O. & Mertz, J. (2000) *J. Opt. Soc. Am. B* **17,** 1685–1694.
35. Hensley, K., Maidt, M. L., Yu, Z., Sang, H., Markesbery, W. R. & Floyd, R. A. (1998) *J. Neurosci.* **18,** 8126–8132.
36. Mahmoud, S. F. & Bialkowski, S. E. (1995) *Appl. Spectrosc.* **49,** 1669–1676.
37. Wrona, M. Z. & Dryhurst, G. (1998) *Chem. Res. Toxicol.* **11,** 639–650.
38. Brown, E. B., Campbell, R. B., Tsuzuki, Y., Xu, L., Carmeliet, P., Fukumura, D. & Jain, R. K. (2001) *Nat. Med.* **7,** 866–870.
39. Guy, C. T., Webster, M. A., Schaller, M., Parsons, T. J., Cardiff, R. D. & Muller, W. J. (1992) *Proc. Natl. Acad. Sci. USA* **89,** 10578–10582.
40. Ouzounov, D. G., Moll, K. D., Foster, M. A., Zipfel, W. R., Webb, W. W. & Gaeta, A. L. (2002) *Opt. Lett.* **27,** 1513–1515.
41. Zoumi, A., Yeh, A. & Tromberg, B. J. (2002) *Proc. Natl. Acad. Sci. USA* **99,** 11014–11019.